JGR Biogeosciences

RESEARCH ARTICLE
10.1029/2019JG005117

El Niño-Southern Oscillation-Induced Variability of Terrestrial Gross Primary Production During the Satellite Era

Yulong Zhang[1,2], **Matthew P. Dannenberg**[3], **Taehee Hwang**[4], **and Conghe Song**[1,2]

[1]Department of Geography, University of North Carolina at Chapel Hill, Chapel Hill, NC, USA, [2]Institute for the Environment, University of North Carolina at Chapel Hill, Chapel Hill, NC, USA, [3]Department of Geographical and Sustainability Sciences, University of Iowa, Iowa City, IA, USA, [4]Department of Geography, Indiana University, Bloomington, IN, USA

Key Points:
- The composite ONI in the previous-year's August-October shows the strongest correlation with global annual GPP
- ENSO effects on annual GPP exhibit diverse seasonal evolutions, and the timing of peak ENSO influences are heterogeneous across the globe
- TRENDY ensemble appears to miss the major lag effects of ENSO identified in the satellite-derived GPP and top-down-based land carbon sink

Supporting Information:
- Supporting Information S1

Correspondence to:
Y. Zhang and C. Song,
ylzhang@unc.edu;
csong@email.unc.edu

Citation:
Zhang, Y., Dannenberg, M. P., Hwang, T., & Song, C. (2019). El Niño-Southern Oscillation-induced variability of terrestrial gross primary production during the satellite era. *Journal of Geophysical Research: Biogeosciences*, *124*, 2419–2431. https://doi.org/10.1029/2019JG005117

Received 27 FEB 2019
Accepted 27 JUN 2019
Accepted article online 12 JUL 2019
Published online 3 AUG 2019

Abstract Terrestrial gross primary production (GPP) is the largest carbon flux entering the biosphere from the atmosphere, which serves as a key driver of global carbon cycle and provides essential matter and energy for life on land. However, terrestrial GPP variability is still poorly understood and difficult to predict, especially at the annual scale. As a major internal climate oscillation, El Niño-Southern Oscillation (ENSO) influences global climate patterns and thus may strongly alter interannual terrestrial GPP variation. Using a remote sensing-driven ecosystem model with long-term satellite and climate data, we comprehensively examined the impacts of ENSO on global GPP dynamics from 1982 to 2016, focusing on lag effects of ENSO and their spatial heterogeneity. We found a clear seasonal lag effect of previous-year ENSO indices on current-year global GPP variability. The composite Oceanic Niño Index in the previous-year's August-October showed the strongest correlation with global annual GPP ($R = -0.51$, $p < 0.01$). Spatially, 20.1% and 11.7% of vegetated land area showed significant negative and positive correlations with the ENSO cycle, respectively. ENSO effects on annual GPP exhibited diverse seasonal evolutions, and the timings of peak ENSO influences were heterogeneous across the globe. Annual GPP from TRENDY land surface model ensemble did not capture the major lag effects of ENSO identified in the satellite-derived GPP and top-down-based land sink. Despite the complexity of the climate system, our efforts linking ENSO with global GPP dynamics provide a simple framework to understand and project climatic influences on the terrestrial carbon cycle.

1. Introduction

Terrestrial gross primary production (GPP) quantifies the total amount of carbon fixed by plants from the atmosphere through photosynthesis (Running et al., 2004). As the largest carbon flux entering the biosphere, terrestrial GPP serves as a major driver of the global carbon cycle (Beer et al., 2010) and a key mechanism to partially offset anthropogenic CO_2 emissions (Houghton, 2007). In addition, terrestrial GPP provides essential matter and energy for all ecosystems (Chapin et al., 2002), supporting the base of the terrestrial food chain (Waring & Running, 2010). However, global terrestrial GPP is still one of the most uncertain variables in Earth's carbon budget (Le Quéré et al., 2018; Running et al., 2004), particularly the dynamics and drivers of its interannual variability (Anav et al., 2015; Campbell et al., 2017; Jung et al., 2017; Luo et al., 2015; Welp et al., 2011).

The El Niño-Southern Oscillation (ENSO) is the periodic fluctuation between anomalously warm (El Niño) and cold (La Niña) sea surface temperatures (SSTs) in the tropical Pacific driven by interactions between atmospheric and oceanic circulations (McPhaden et al., 2006). Coupled with tropical atmospheric circulations and other pervasive teleconnections (Wang & Picaut, 2004), ENSO exerts a major influence on climate patterns across the world (McPhaden et al., 2006). During El Niño events, most of Earth's land surface tends to be much warmer and drier than normal, particularly in tropical regions (Dai & Wigley, 2000). Other regions, such as western North America (Ropelewski & Halpert, 1986) and East Asia (Wu et al., 2003), tend to be cooler and wetter. La Niña generally shows opposite influences on surface climate (Diaz et al., 2001). Overall, climate influences of ENSO vary regionally and depend on the strength and timing of SST anomalies (Dai & Wigley, 2000; Diaz et al., 2001). Given that El Niño and La Niña recur periodically (usually every 2 to 7 years), the global climate variability induced by ENSO could strongly

shape terrestrial GPP dynamics and appears to be a major source of interannual GPP variability (Hashimoto et al., 2004; Jones et al., 2001).

In general, global GPP tends to be lower than normal during El Niño years (Bastos et al., 2018), and vice versa in La Niña years (Bastos et al., 2013). However, the heterogeneous relationships between climate variability induced by ENSO and terrestrial ecosystem productivity, especially regarding the extent, amplitude, and underlying mechanisms, are still not well understood (Gonsamo et al., 2016; Wang et al., 2018; Zhu et al., 2017). Previous studies have been largely conducted at regional (Dannenberg et al., 2015; Moore et al., 2018; Parazoo et al., 2015) or continental scales (Baker et al., 2010; Ciais et al., 2009; Zhang et al., 2017). Global-scale studies were mainly based on the short MODIS record (Bastos et al., 2013; Luo et al., 2018), only normalized difference vegetation index rather than estimated GPP (Gonsamo et al., 2016; Kogan & Guo, 2017), or solely based on modeled results with no remote sensing inputs (Ahlström et al., 2015; Zhu et al., 2017). Some global-scale studies based on various sources of GPP models were mainly focused on only a small sample of El Niño/La Niña events (Bastos et al., 2018; Wang et al., 2018). In addition, most of these studies investigated ENSO influences with either a fixed ENSO period (typically during northern hemisphere winter) or with lag effects that were fixed at a few equal-interval periods (e.g., 3 or 6 months; Gonsamo et al., 2016; Zhu et al., 2017).

Coupling ecosystem models and remotely sensed observations, each with complementary strengths and weaknesses, provides a promising way to explore global GPP dynamics and its linkage with ENSO (Anav et al., 2015; Beer et al., 2010). The Advanced Very High Resolution Radiometer (AVHRR) sensors onboard the National Oceanic and Atmospheric Administration (NOAA) satellite series provide the longest continuous spectral measurements on the land surface since 1981 (Pettorelli et al., 2005). Based on the combined use of long-term AVHRR data (Zhu et al., 2013) and a newly developed ecosystem model (Zhang et al., 2016; Zhang et al., 2019), we comprehensively examined the impacts of ENSO on global GPP dynamics from 1982 to 2016. The specific aims of our study are (1) to explore the time-lag effect of ENSO on annual GPP variation and its spatial heterogeneity, (2) to quantify how the diverse GPP responses to ENSO across climatic zones determined the global GPP anomaly, and (3) to test if land surface models without remote sensing inputs (i.e., TRENDY) showed comparable ENSO effects on global GPP as the remote sensing-driven model. Our study linking the ENSO cycle to spatiotemporal variations of GPP could improve our understanding of interannual variability and climatic drivers of global GPP, potentially leading to improvements of both short-term forecasts of vegetation productivity and longer-term projections of climatic influences on the carbon cycle.

2. Data and Methods

2.1. Teleconnection Indices

SST anomalies over the tropical Pacific Ocean are usually used to quantify the state of ENSO. In this study, we constructed an Oceanic Niño Index (ONI; https://ggweather.com/enso/oni.htm) as the 3-month running mean SST anomaly for the Niño 3.4 region (i.e., 5° N–5° S, 120–170° W). We first obtained the original monthly SST values from NOAA's Extended Reconstructed Sea Surface Temperature (ERSST) V5 data set over this region from 1980 to 2016. To better reflect interannual ENSO variability, we detrended the monthly ONI by removing the mean seasonal cycles and long-term trends and then calculated the 3-month running mean ONI anomalies during the study period.

In addition to ENSO, previous studies have shown that the Atlantic Multidecadal Oscillation (AMO) and Pacific Decadal Oscillation (PDO) can also influence land surface climate (Wise, 2010) and global carbon fluxes (Zhu et al., 2017). Therefore, we also included these two teleconnection patterns in our study. The monthly indices for AMO and PDO from 1980 to 2016 were downloaded from NOAA (http://esrl.noaa.gov/psd/) and the University of Washington (http://research.jisao.washington.edu/pdo/), respectively. Given that PDO and AMO have already been detrended, we simply constructed their 3-month running means similar with ONI.

2.2. Global GPP Data Set

We estimated terrestrial GPP based on a newly developed ecosystem model, the Coupled Carbon and Water (CCW) model (Zhang et al., 2016; Zhang et al., 2019). This model estimates GPP based on light-use efficiency theory and accounts for biome-specific environmental constraints, such as low/high temperature, moisture

stress, and light saturation. Using the up-to-date global eddy covariance flux tower data (i.e., FLUXNET2015), the version of CCW used in this study has been comprehensively calibrated and evaluated and can be effectively applied over large scales (Zhang et al., 2019).

Based on CCW, we estimated global GPP at a monthly scale with a spatial resolution of 1/12° from 1982 to 2016. Global inputs for CCW included monthly fraction of photosynthetically absorbed radiation (FPAR) derived from AVHRR GIMMS NDVI3g based on an artificial neural network (Zhu et al., 2013), land use and land cover data from MODIS (2001; Friedl et al., 2002), and climate data (i.e., solar radiation, air temperature, and vapor pressure deficit [VPD]) from CRU-NCEP (Viovy, 2018). The GIMMS leaf area index (LAI; Zhu et al., 2013) and CRU-NCEP precipitation (Viovy, 2018) were also used for subsequent analyses. To match the spatial resolution of the GIMMS FPAR3g, we rescaled the 0.5° CRU-NCEP data using bilinear interpolation and aggregated the 1-km MODIS land cover data based on the majority rule in each 1/12° pixel.

To compare our results with other global GPP models, we used global GPP simulations during the study period from 16 land surface models in the TRENDY V6 ensemble (Bastos et al., 2018; Sitch et al., 2015). The selected models are shown in supporting information Table S1. We also derived annual land carbon sink during the same period using a top-down approach, that is, the balance of atmospheric CO_2 growth rate, CO_2 emissions from fossil fuel combustion and land use change, and ocean carbon sink from the Global Carbon Budget 2017 (Le Quéré et al., 2018).

2.3. Analysis Methods

To separate the net effect of climate variations from other long-term factors, such as atmospheric CO_2 fertilization, nitrogen deposition, and land use change, we detrended all the annual data including GPP, greenness indicators (FPAR and LAI), and climate at the pixel level by removing their long-term linear trends. We then examined the seasonal patterns of ENSO influences on annual GPP anomalies using correlation analysis. Pearson's correlation coefficients were calculated between annual GPP and the 3-month running means of ONI during the 24-month period starting from the previous calendar year through the current calendar year (hereafter the month of ONI is referred to as the "ending month": e.g., ONI in September is the composite ONI from July to September). The time of strongest ENSO influence on annual GPP (hereafter referred to as "peak time") was identified by the maximum correlation coefficient (hereafter referred to as "peak correlation") both at the global and pixel scales. To identify the likely proximate drivers of ENSO influences at the peak time, we also calculated the correlations between ONI and potential GPP derivers (i.e., climate, LAI, and FPAR). To better reflect the seasonal evolution of ENSO effects on GPP at the plot level, we randomly selected 14 sites across different climate zones in both hemispheres (Figure S1 and Table S2).

To identify the major El Niño and La Niña years, we calculated annual integrated ONI from July in the previous year to May in the current year when ENSO signals showed significant correlations with global GPP ($p < 0.05$; shown in section 3.1). We identified five La Niña years with annual ONI < -1.0 (i.e., 1989, 1999, 2000, 2008, and 2011) and four El Niño years with annual ONI > 1.0 (i.e., 1983, 1992, 1998, and 2016), all of which were labeled as "strong" or "very strong" ENSO events according to NOAA's classification (https://ggweather.com/enso/oni.htm). We then calculated multiyear averaged GPP anomalies from all those major El Niño and La Niña years and then compared their spatial patterns.

To compare the results based on the CCW model, we conducted similar correlation analyses on lag effects of ENSO on global annual GPP from the TRENDY ensemble and land carbon sink from Global Carbon Budget. To control the potential effects of PDO and AMO, we further repeated the lag effect analysis for global annual GPP from both CCW and TRENDY and land sink using partial correlation analyses (dependent factor: GPP/land sink; independent factor: ONI; control factors: PDO and AMO).

3. Results

3.1. Long-Term GPP Dynamics Linked With ENSO

Global detrended GPP from CCW showed considerable variability with a standard deviation (SD) of 1.66 Pg C/year from 1982 to 2016 (Figure 1a). Positive anomalies of annual GPP were registered in all five strong La Niña years (1989, 1999, 2000, 2008, and 2011), while negative GPP anomalies appeared in two (1983 and 2016) of four strong El Niño years. In the strong El Niño year of 1998, annual GPP was slightly above average, but this still represented a large reduction compared to the previous year (−1.73 Pg C/year or −87.8%).

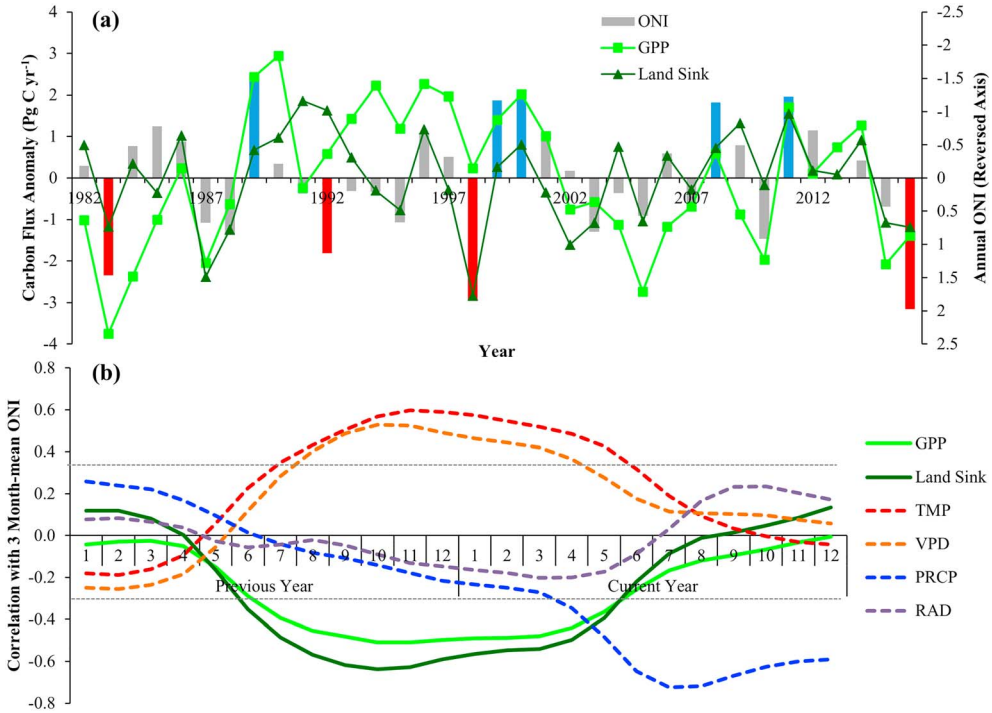

Figure 1. Interannual variability of global carbon fluxes linked with El Niño-Southern Oscillation from 1982 to 2016 (a) and lag effects of El Niño-Southern Oscillation on global carbon fluxes and climate variables (b). Annual ONI in (a) is the annual mean of monthly ONI from preceding July to current May, shown with a reversed axis. Red bars represent strong El Niño years with ONI > 1, while blue bars represent strong La Niña years with ONI < −1. Annul GPP here was simulated by the CCW model while land carbon sink from Global Carbon Budget. The correlations in (b) represent Pearson correlation coefficients of 3-month average ONI from the previous to current years with other current annual climate variables, such as RAD, TMP, PRCP, and VPD. Two horizontal dotted gray lines indicate the 95% significance level. RAD = radiation; TMP = air temperature; PRCP = precipitation; VPD = vapor pressure deficit; ONI = Oceanic Niño Index; GPP = gross primary production.

Overall, the strong El Niño year of 1983 corresponded to the highest negative GPP anomaly (−3.75 Pg C/year or −2.3 SD), while the strong La Niña year of 1989 was linked with the second largest positive GPP anomaly (i.e., 2.43 Pg C/year or +1.5 SD). Notably, the CCW-modeled global GPP also showed a significant correlation with land carbon sink data during the study period (R = 0.42; p < 0.01; Figure 1a), which appeared to have a similar association with El Niño and La Niña events (Figure 1a).

3.2. Lag Effects of ENSO on Global GPP Variability

ENSO showed a clear lag effect on global annual GPP variability from the previous year to the current year (Figure 1b). The correlation between ONI and annual GPP appeared to be significantly negative (p < 0.05) starting in July of the previous year. After that, the strength of the correlation soon reached its peak in October of the previous year (R = −0.51, p < 0.01) and stayed nearly stable until March of the current year. After that, the correlation strength started to sharply decrease, becoming insignificant in June of the current year. A similar ENSO influence but with an opposite sign was found in both global annual air temperature (highest R = 0.60, p < 0.01) and VPD (highest R = 0.53, p < 0.01). Interestingly, annual total precipitation appeared to be most strongly associated with ONI in July of the current year, absent of the lag effect seen in GPP. ENSO signals did not significantly correlate with global total surface radiation. During the study period, ENSO showed similar but slightly stronger significant effects on land carbon sink when compared with GPP (Figure 1b).

3.3. Spatial Heterogeneity of ENSO Effects on GPP

Based on the seasonal evolution of ENSO effects (Figure S2), we derived the spatial pattern of the peak correlation between the annual GPP and monthly composite ONI during the previous year to current year (Figure 2a). Annual GPP showed diverse responses to ENSO signals across different regions. Strong negative correlations between ONI and GPP (p < 0.05) were mainly observed in the tropics and southern hemisphere,

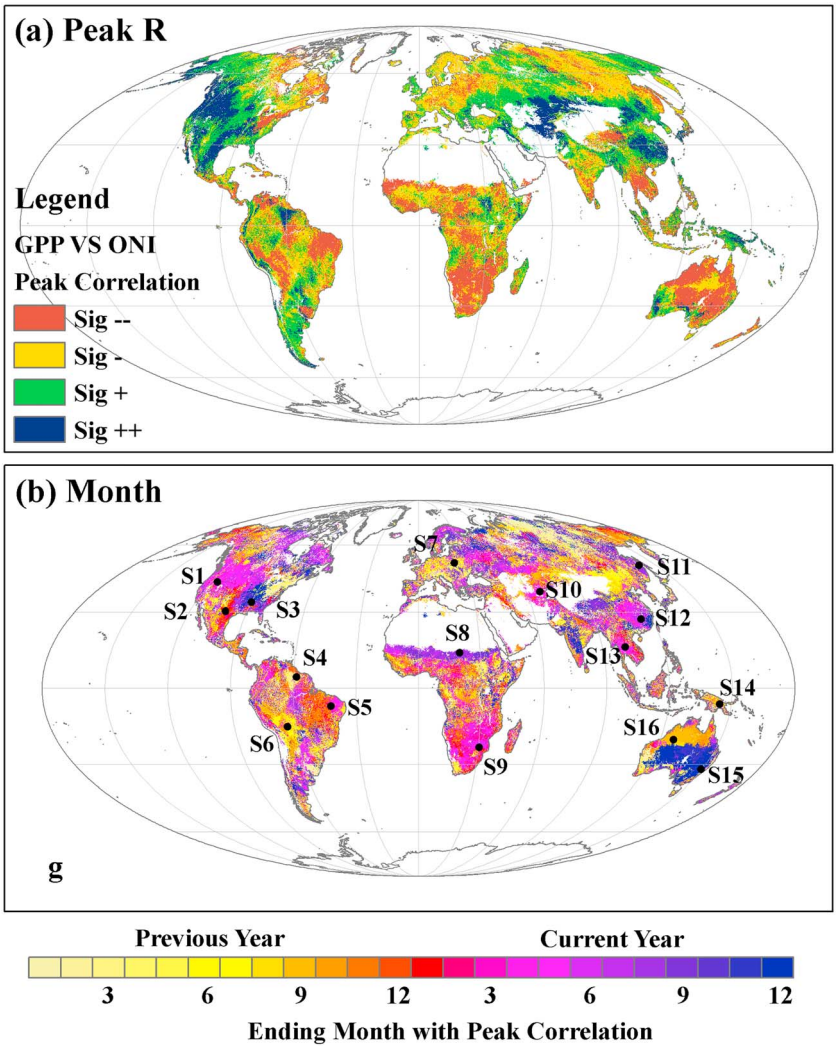

Figure 2. Spatial patterns of El Niño-Southern Oscillation effects on annual GPP variability in terms of the peak correlation (a) and the corresponding time (b). The legends Sig ++ and Sig −− in (a) indicate significant positive and negative correlations ($p < 0.05$), respectively, while Sig + and Sig − represent nonsignificant correlations ($p > 0.05$). ONI = Oceanic Niño Index; GPP = gross primary production.

particularly in Africa, Australia, central South America, and south Asia, while strong positive correlations ($p < 0.05$) were mostly clustered in midlatitude northern hemisphere such as central and western North America, central Asia, and southern China. Globally, 20.1% of land vegetated area exhibited significant negative linkage with ONI, composed of arid (7.0%), tropical (6.6%), boreal (3.8%), and temperate (2.7%) zones. By comparison, 11.7% of land area showed significant positive ONI linkage, composed of arid (3.9%), temperate (3.2%), boreal (3.0%), and tropical (1.5%) zones.

The time corresponding to the peak correlation (or peak time) showed a heterogeneous spatial pattern (Figure 2b). Peak time in the previous year suggests a strong lag effect of ENSO on annual GPP. These regions accounted for 41% of the total land area with significant correlations ($p < 0.05$), which mainly occurred in the tropical regions, central Asian, and northern Australia. Peak time in the current year indicates a more synchronous coupling of ENSO with GPP. This pattern occurred throughout much of the temperate, arid, and boreal regions. Overall, the ONI signals of the current year's March-May and previous year's September-November were two major seasons with the strongest correlations with the annual GPP, which accounted for 22% and 16% of the total significant land area ($p < 0.05$; Figure S3), respectively. However, the typical northern hemisphere "winter" season (i.e., December-February) was only responsible for 8% of the total significant peak correlations (Figure S3), which mainly appeared in central tropics and parts of

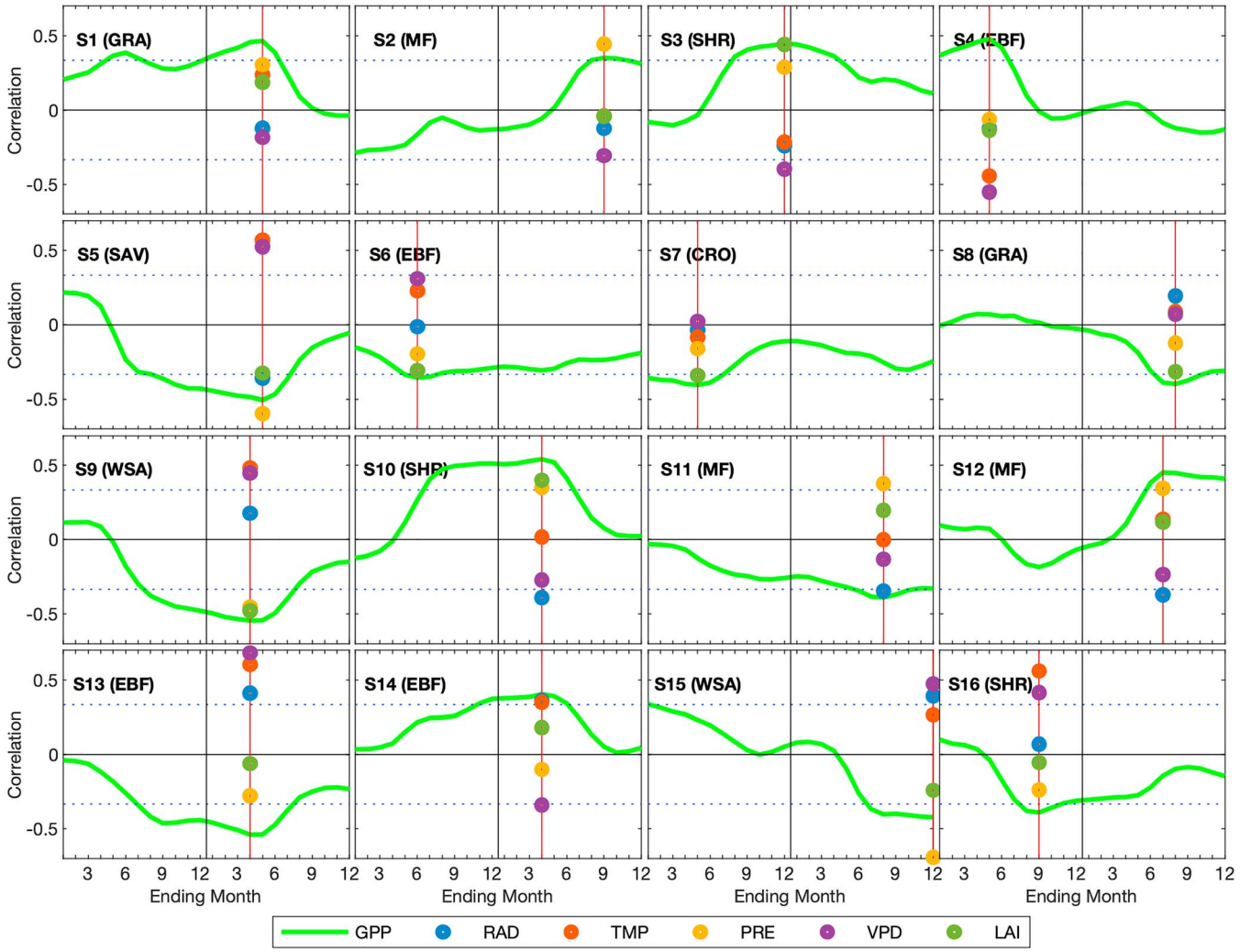

Figure 3. Seasonal evolution of El Niño-Southern Oscillation effects on annual GPP in terms of correlation at randomly selected sites. The red vertical line indicates the peak correlation during the previous to current years. The location of each site was shown in Figure 2b. Other site information including climate zones and biome types were seen in Table S2. Two horizontal dotted lines indicate the 95% significance level. GPP = gross primary production; RAD = radiation; TMP = air temperature; PRE = precipitation; VPD = vapor pressure deficit; LAI = leaf area index.

arid/semiarid regions. Of note, about 7% of the total significant peak correlations occurred at the end of the current year (i.e., December), which were mainly seen in the southern Australia and represented synchronous coupling of the ENSO system with the southern hemisphere growing season.

The seasonal evolution of ENSO effects on GPP was more diverse at the plot scale (Figure 3). The randomly selected 14 sites across different climate zones and vegetation types (Figure 2b and Table S2) exhibited quite different seasonal trajectories and peak time in their linkage between ENSO and GPP (Figure 3). For example, two tropical sites in Asia (S13 and S14) showed the same peak time but opposite seasonal trajectories. In contrast, two tropical sites in South America (S3 and S4) showed similar seasonal trajectories but quite different peak times. Other pairs of arid sites (S2 and S7), boreal sites (S1 and S11), and temperate sites (S10 and S12) all showed different seasonal trajectories with different peak times.

3.4. Underlying Mechanisms of ENSO Effects on GPP

ENSO was intrinsically linked with GPP through its effects on surface climate variability and canopy structural change (Figures 3 and 4). At the peak correlation time with GPP, the ONI showed significant correlations with annual total surface radiation, air temperature, and total precipitation over 10.2%, 24.8%, and

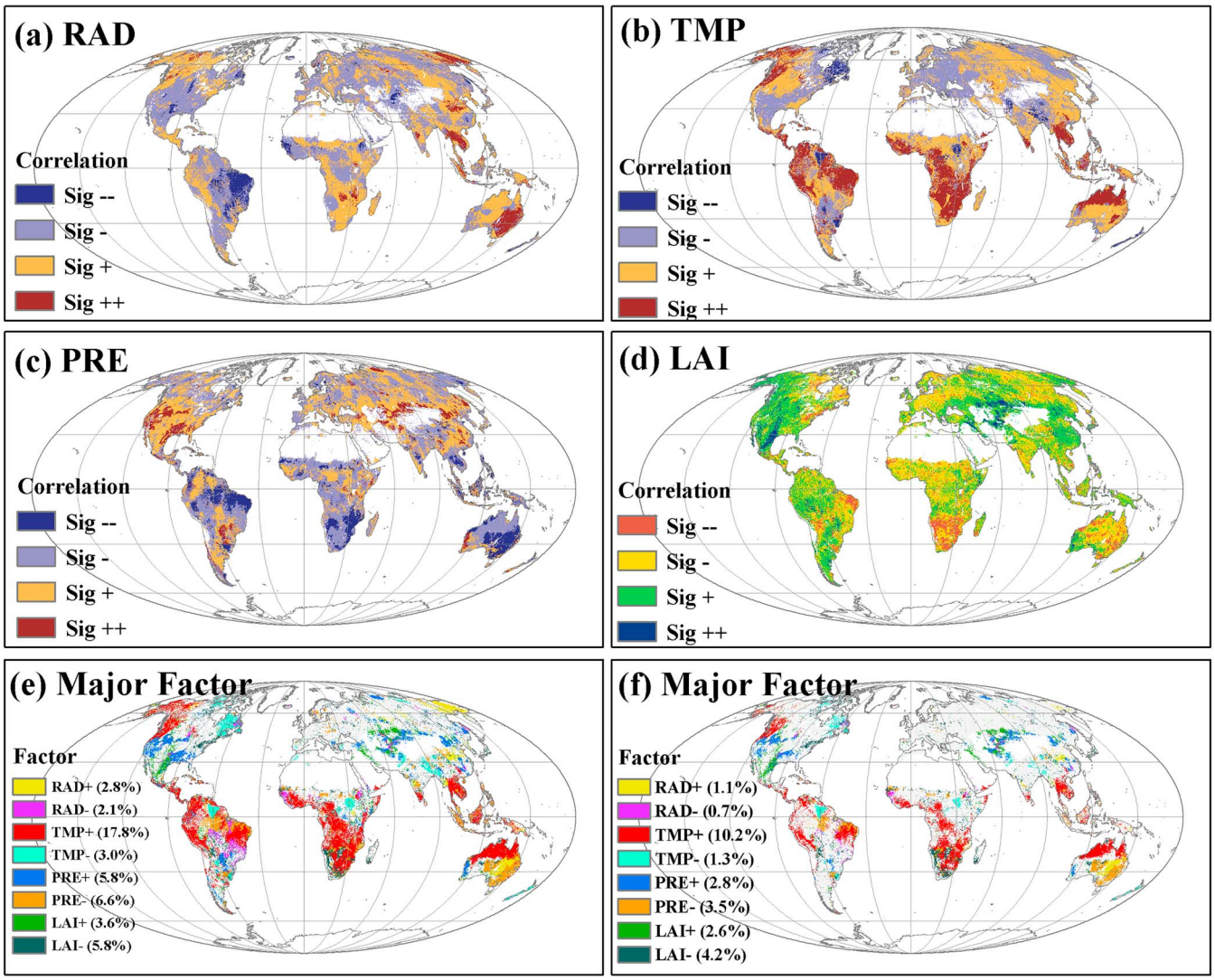

Figure 4. Spatial patterns of El Niño-Southern Oscillation effects on climate variables and greenness index at the peak time (Figure 2). Climate variables included (a) annual total surface RAD, (b) surface TMP, and (c) surface total PRE. The legends Sig ++ and Sig −− in (a)–(d) indicate significantly positive and negative correlations with $p < 0.05$, respectively, while Sig + and Sig − insignificantly correlations with $p > 0.05$. Major factors in (e) were identified by comparing correlations of Oceanic Niño Index with factors in (a)–(d). The insignificant correlations in (e) were masked as gray color. According to insignificant El Niño-Southern Oscillation influences in Figure 2a, major factors in (e) were further masked to yield the subfigure in (f). The values in legend parentheses in (e) and (f) show the area relative to total vegetated land area. RAD = radiation; TMP = air temperature; PRE = precipitation; VPD = vapor pressure deficit; LAI = leaf area index.

18.4% of global vegetated area, respectively (Figure 4). ENSO-induced variability in temperature and precipitation further affected annual VPD variations over 21.2% of land area (Figure S4). As a result, 14.3% of land area exhibited significant correlations between ONI and annual mean LAI (Figure 4d), which further determined the potential rate of photosynthesis through FPAR (Figure S4). Overall, ENSO-induced climate and canopy structure changes occurred over 47.5% of vegetated land area (Figure 4e), of which 55.5% were identified to directly influence annual GPP variability (Figure 4f). Among those major GPP influencing factors, the composite ONI tended to positively correlate with annual temperature (10.2% of total area) but negatively correlate with annual precipitation (3.5% of total area) and LAI (4.2% of total area; Figure 4f).

3.5. Average GPP Anomalies in El Niño and La Niña Years

Multiyear averaged GPP anomalies (Figure 5) were derived from all strong El Niño and La Niña years (Figure S5). As expected, annual GPP anomalies showed quite different spatial patterns in the two events,

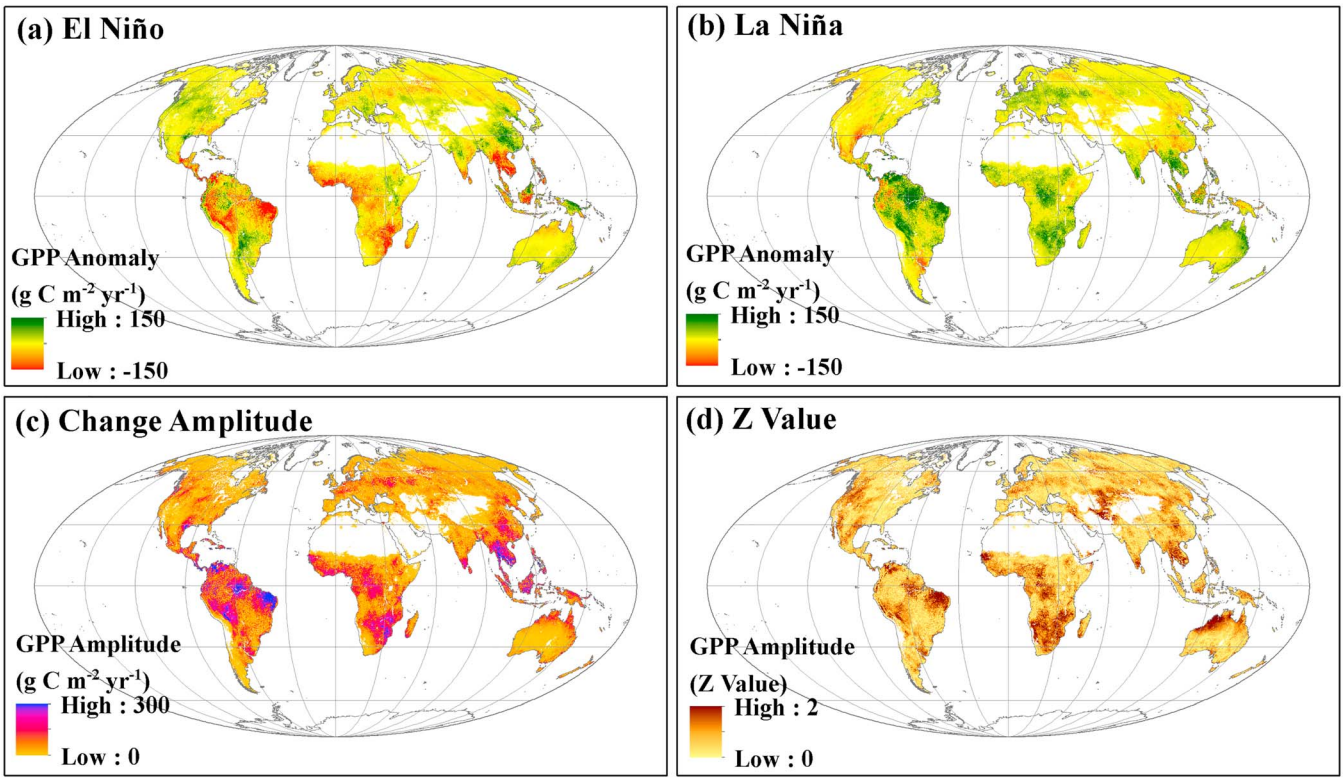

Figure 5. Spatial patterns of multiyear averaged GPP anomalies in El Niño (a) and La Niña (b) years, and their change amplitudes (c–d). The separate annual anomaly data were seen in Figure S5. (c) is the change amplitude between (a) and (b). (d) is the Z value indicating the ratio of the change amplitude in (c) relative to the multiple-year GPP standard deviation during the study period. GPP = gross primary production.

and the identified strong ENSO effect regions (Sig ++ and Sig −− seen in Figure 2a) tended to exhibit higher GPP fluctuations (Figure 5). For the El Niño years, the negative and positive ENSO effect areas, respectively, showed total GPP anomalies of −1.62 and 0.54 Pg C/year, resulting in a total negative global GPP anomaly of −1.08 Pg C/year (Table S2). In contrast, for the La Niña years, the same two kinds of areas, respectively, exhibited total GPP anomalies of 1.90 and −0.26 Pg C/year, together yielding a positive global GPP anomaly of 1.63 Pg C/year (Table S2). Overall, El Niño/La Niña tended to influence the global GPP anomaly primarily through tropical and arid/semiarid regions, whereas temperate and boreal regions, to some degree, buffered the negative effects of El Niño and positive effects of La Niña on global GPP (Figure 5 and Table S3).

3.6. Comparison of ENSO Effects on Global GPP From CCW and TRENDY

The seasonal evolution of ENSO effects on global annual GPP variability showed a relatively large discrepancy between CCW and TRENDY (Figure 6a). Among 16 TRENDY models, six models did not show any significant correlations between global annual GPP and monthly ONI from the previous to the current years (Figure S6). The remaining models exhibited significant linkages between GPP and ONI mainly in June-July of the previous year or May-August of the current year (Figure S6). However, the strong ENSO effects from August of the previous year to April of the current year identified by CCW and by the top-down Global Carbon Budget were not reflected in TRENDY (Figures 6 and S6). Controlling the possible effects of teleconnections from AMO and PDO did not decrease this discrepancy (Figure 6b). During the study period, global annual GPP from the ensemble mean of TRENDY was not significantly correlated with annual GIMMS LAI3g ($R = -0.22$, $p > 0.05$) and land carbon sink ($R = 0.23$, $p > 0.05$), which is different from CCW GPP (i.e., exhibiting strong correlations with LAI3g [$R = 0.77$, $p < 0.01$] and land sink [$R = 0.42$, $p < 0.01$]; Figure S7). Regional differences in ENSO effects from CCW and TRENDY are shown in Figures S8 and S9. Overall, TRENDY was less responsive to ENSO in tropical and arid/semiarid regions compared to CCW (Figure S8).

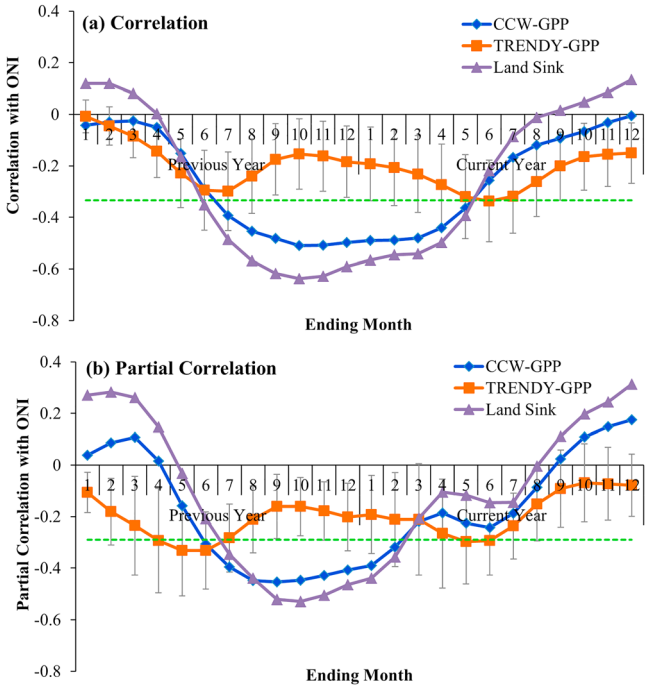

Figure 6. Comparisons of the lag effects of El Niño-Southern Oscillation on annual GPP from CCW and TRENDY models and top-down approach-based land sink. (a) Simple correlation of the composite ONI with annual GPP and land sink; (b) partial correlation by controlling the effects of Atlantic Multidecadal Oscillation and Pacific Decadal Oscillation. Error bars for TRENDY indicated the standard deviations of correlations for the selected 16 models seen in Table S1. The horizontal dotted line indicated the 95% significance level. ONI = Oceanic Niño Index; CCW = Coupled Carbon and Water; GPP = gross primary production.

4. Discussion

Global GPP estimated by the CCW model exhibited considerable interannual variability over the past 35 years (Figure 1a). However, we showed that ENSO fluctuations explained up to 26% of interannual variation in global GPP ($p < 0.01$), with below average GPP following strong El Niño years but above average following strong La Niña years (Figure 1b). We also found substantial lags between ENSO conditions and their influence on terrestrial GPP, suggesting the potential for forecasting terrestrial vegetation productivity based on ENSO indices in advance of the growing season. Previous studies usually adopted the boreal winter season index to assess the influence of ENSO on global vegetation productivity, given that the ENSO amplitude (i.e., the actual tropical SST variability) tends to be greatest at that time (Bastos et al., 2013; Dannenberg et al., 2015; Gonsamo et al., 2016). However, we showed that the boreal winter season is not the only time window to exhibit significant influence on global GPP nor is it necessarily the season with the strongest influence on terrestrial GPP. In contrast, ENSO cycles are significantly correlated with global GPP as early as July of the previous year, with peak in October of the previous year (Figure 1b). Such a relationship could be used to forecast global annual GPP anomalies up to 9 months prior to the growing season, though the timing of the lag effect varies regionally (Figure 2). Given ENSO could be forecasted within a range of 1 to 9 months in advance (Tippett et al., 2012), such a prediction for global GPP could be even earlier.

Spatially, ENSO exhibited contrasting influences on annual GPP anomalies (Figure 2a), with a greater proportion of the land surface responding negatively (61%) than positively (39%) to the ONI. Therefore, ENSO-induced GPP anomalies in some regions could be partially compensated by the opposite GPP response in other regions (Bastos et al., 2018; Woodward et al., 2008). Our study indicates that, in the strong El Niño years, tropical and arid/semiarid regions tend to be dominated by negative climate impacts on GPP, while temperate and boreal regions partly offset this response, together resulting in overall negative anomalies at the global scale (Figure 5a and Table S2). However, in the strong La Niña years, relatively small negative GPP anomalies mainly from temperate and boreal regions are largely overcome by positive GPP anomalies in tropical and arid/semiarid regions, yielding a strong positive anomaly in global GPP (Figure 5b and Table S2). Overall, the long-term satellite-driven data clearly depict the spatial association between ENSO events and global GPP anomalies and highlight tropical and arid/semiarid regions as the most sensitive regions to ENSO (Ahlström et al., 2015; Hashimoto et al., 2004; Hilker et al., 2014; Piao et al., 2009).

The linkage of ENSO with global annual GPP fluctuations appeared to be mainly via its influences on temperature and thus VPD but less from other factors (Figure 2b). For precipitation and incoming radiation, this is likely due to the aggregation of regional anomalies with opposite signs, which cancel each other out at the global scale, whereas the temperature and VPD responses to ENSO tend to be more ubiquitous across Earth's land surface. However, the mechanisms behind the linkage between GPP and ENSO are much more complex at regional scales (Figure 4). Given that CCW is not a general circulation model that integrates the physical links between ENSO and climate (Guilyardi et al., 2009), we could not directly separate ENSO-induced climate influences on GPP using traditional factorial experiments to minimize covariance effects of climate variables (e.g., Piao et al., 2009). However, the empirical correlation analysis in our study identified close linkages between ENSO and dominant climatic and canopy structural variables, which appeared to be coresponsible for diverse GPP responses across different climate zones (Figures 4 and S4). Of note, temperature-related water stress (controlled by a combination of temperature, VPD, and precipitation) is a major driver of ENSO-induced regional GPP variability, especially in tropical and arid/semiarid areas (Ahlström et al., 2015; Hashimoto et al., 2004; Hilker et al., 2014; Humphrey et al., 2018). Canopy greenness indices such as LAI and FPAR appeared to be less responsive to ENSO (Figures 4d and S4b), indicating that

they may not fully reflect the linkage of GPP with ENSO without explicitly accounting for climate constraints (Gonsamo et al., 2016; Woodward et al., 2008; Zhang et al., 2015).

As the most prominent driver of year-to-year internal climate variation on Earth, ENSO carries several characteristics such as nonlinearity, seasonality, and memory effects (Chen et al., 2016), which may shape its influences on GPP. We showed that ENSO effects on annual GPP exhibited diverse seasonal evolutions across Earth's ecosystems (Figures 3 and S2), and the times for the maximum influences were heterogeneous worldwide (Figure 2b). This also indicates that attempts at forecasting annual GPP based on boreal winter ONI may not be successful in some regions if the peak time for ENSO influence occurs at a different time. Our results suggest that ENSO could be a valuable tool for forecasting annual ecosystem productivity variation, particularly if the time lags used for forecasting are optimized for the specific region of interest. In some regions, on the other hand, forecasting based on ENSO may be less successful due to short lag times between ENSO and ecosystem GPP. For example, some arid and semiarid regions, such as those in southern Australia, showed peak time in the boreal winter/austral summer of the current year (Figure 2b), demonstrating synchronous effects of ENSO on the climate and subsequent GPP. Given the close relationships between GPP and vegetation biomass/yield (Bradford & Crowther, 2013), these types of forecasts identified in our study could also potentially be useful for regional agriculture management, crop yield estimation, and rangeland usage (Chen et al., 2017; Iizumi et al., 2014).

The TRENDY land surface model ensemble has been widely used to explore anomalies of terrestrial carbon fluxes in association with climate change/variation (Ahlström et al., 2015; Sitch et al., 2015; Zhang et al., 2018). However, these land surface models, even driven by observed climate, appeared to miss the major lag effects of ENSO on global annual GPP identified based on the remote sensing-driven GPP simulation (Figure 6a) and the top-down based land sink (Figures 1b and 6a). Our study further confirmed a poor correlation of TRENDY GPP with global GIMMS LAI3g and land carbon sink when compared with CCW (Figure S7). Although sharing the same CRU-NCEP climate inputs, land surface models from the TRENDY ensemble largely underestimate ENSO effects on global GPP compared to CCW, probably due to the lack of constraint from remote sensing inputs (MacBean et al., 2015; Richardson et al., 2012) and/or the model deficiency or biases in representing climatic effects (Anav et al., 2015; Sitch et al., 2015; Wang et al., 2014). This finding agrees with the study by Wang et al. (2014), who found that most land surface models failed to capture the recent enhanced carbon cycle sensitivity to ENSO-related climatic variations. The strong role of temperature (via its nonlinear effects on VPD) revealed in our study reflects the regulation of moisture status on temperature sensitivity of GPP in related to ENSO (Figures 4 and S2), especially in tropical and arid/semiarid regions, which provides further clarification of the processes responsible for the model underestimation of observed climatic sensitivity (Gonsamo et al., 2016; Wang et al., 2014). In addition, the identified seasonal evolution of ENSO effects on GPP in our study could be further used to constrain other land surface models (e.g., CMIP5).

Notably, when controlling for variations of AMO and PDO using partial correlation analyses, seasonal lags between ENSO and global GPP did not change substantially (Figure 6), suggesting the leading role of ENSO over other teleconnections on the global scale (Alexander et al., 2002; Zhu et al., 2017). However, currently, the mechanisms behind how ENSO influences climate variability in or beyond tropics through atmospheric circulations and/or teleconnections are still not very clear (Diaz et al., 2001; Gershunov & Barnett, 1998; Yeh et al., 2018), and ENSO may interact with other teleconnections to coinfluence regional surface climate (Seager et al., 2010; Wise et al., 2015) and vegetation productivity (Dannenberg et al., 2018; Gonsamo et al., 2016; Zhao et al., 2018; Zhu et al., 2017). Future efforts in examining such interactions would help us to better understand ENSO-induced GPP variability.

Variation of the land carbon sink—driven by uptake of CO_2 through GPP and release through ecosystem respiration—was also strongly linked to ENSO (Figures 1 and 6). The highly matched peak times and seasonal trajectories of ENSO effects between annual GPP and the land sink suggest the dominant role of global GPP in determining the response of the land carbon sink to ENSO (Ahlström et al., 2015; Zhang et al., 2018). The slightly stronger peak influence of ENSO on the land sink than on GPP may be caused by the modification of ecosystem respiration, which strongly depends on temperature, moisture condition, and the accumulated substrate available for decomposition (Chen et al., 2015; Migliavacca et al., 2011). The altered land carbon sink by ENSO would further determine the atmospheric CO_2 anomaly (Bastos et al., 2018; Liu

et al., 2017). Despite the complexity of the climate system, we show that ENSO can be used as a simple tool for understanding and predicting climatic influences on global carbon cycles (McPhaden et al., 2006; Zhu et al., 2017). Greenhouse warming could result either in changes in the mean state of ENSO (McPhaden et al., 2006; Vecchi et al., 2008) or in a more variable and extreme ENSO cycle (Cai et al., 2014; Cai et al., 2015; Power et al., 2013), though there is still substantial uncertainty around the direction and magnitude of changes due to the complexity of atmospheric and oceanic feedbacks (Collins et al., 2010). Given the global effect of ENSO on GPP identified by our study, such future changes of ENSO may strongly influence terrestrial ecosystem productivity and thus the global carbon cycle and its feedbacks to the climate system (Friedlingstein, 2015; Kim et al., 2017).

5. Conclusions

Based on a remote sensing-driven GPP model and global climate data, we comprehensively examined the impacts of ENSO on long-term global GPP variability, focusing on the time-lag effect and its spatial heterogeneity. We found a clear seasonality of ENSO influences on global GPP variability, with peak correlations occurring between global annual GPP and ENSO conditions during August-October of the previous year ($R = -0.51$, $p < 0.01$). Spatially, 20.1% and 11.7% of land vegetated area exhibited significantly negative and positive correlations to ONI, respectively. ENSO effects on annual GPP exhibited diverse seasonal evolutions across Earth's land surface, with high regional variation in the timing of peak ENSO influence on GPP. ENSO was intrinsically linked with the variability of major climate and canopy structural changes that potentially regulated GPP. Overall, El Niño and La Niña tended to influence global GPP anomalies primarily through tropical and arid/semiarid regions, though temperate and boreal regions, to some degree, buffered the negative effects of El Niño and positive effects of La Niña on global GPP. Compared to the remote sensing-derived GPP estimates, annual GPP from the TRENDY land surface model ensemble appeared to largely underestimate the influence of ENSO on global GPP and missed the major lag effects of ENSO. Despite the complexity of the climate system, our results suggest that annual GPP dynamics can be predicted months in advance of the growing season for many regions based on ENSO conditions, thus providing a simple framework for understanding and forecasting climatic influences on the terrestrial carbon cycle.

Acknowledgments
We thank Dr. Zaicun Zhu for providing GIMMS LAI/FPAR3g, the Dynamic Global Vegetation Model Project team for providing TRENDY V6 data, the Global Carbon Project Science Team for providing the global carbon budget data, and Dr. Nicolas Viovy for providing the global CRU-NCEP climate data. This study was supported by NASA Carbon Cycle Science (NNX17AE69G). All data needed to evaluate the conclusions are referenced in the paper and/or the supporting information. The generated global GPP anomaly product can be accessed at the platform of Open Science Framework (https://osf.io/mqg9r/?view_only=27a598289c58410abb504969466a4018).

References

Ahlström, A., Raupach, M. R., Schurgers, G., Smith, B., Arneth, A., Jung, M., et al. (2015). The dominant role of semi-arid ecosystems in the trend and variability of the land CO_2 sink. *Science*, *348*(6237), 895–899. https://doi.org/10.1126/science.aaa1668

Alexander, M. A., Bladé, I., Newman, M., Lanzante, J. R., Lau, N.-C., & Scott, J. D. (2002). The atmospheric bridge: The influence of ENSO teleconnections on air–sea interaction over the global oceans. *Journal of Climate*, *15*(16), 2205–2231. https://doi.org/10.1175/1520-0442(2002)015<2205:TABTIO>2.0.CO;2

Anav, A., Friedlingstein, P., Beer, C., Ciais, P., Harper, A., Jones, C., et al. (2015). Spatiotemporal patterns of terrestrial gross primary production: A review. *Reviews of Geophysics*, *53*, 785–818. https://doi.org/10.1002/2015RG000483

Baker, I., Denning, S., & Stöckli, R. (2010). North American gross primary productivity: Regional characterization and interannual variability. *Tellus Series B: Chemical and Physical Meteorology*, *62*(5), 533–549. https://doi.org/10.1111/j.1600-0889.2010.00492.x

Bastos, A., Friedlingstein, P., Sitch, S., Chen, C., Mialon, A., Wigneron, J.-P., et al. (2018). Impact of the 2015/2016 El Niño on the terrestrial carbon cycle constrained by bottom-up and top-down approaches. *Philosophical Transactions of the Royal Society, B: Biological Sciences*, *373*(1760), 20170304. https://doi.org/10.1098/rstb.2017.0304

Bastos, A., Running, S. W., Gouveia, C., & Trigo, R. M. (2013). The global NPP dependence on ENSO: La Niña and the extraordinary year of 2011. *Journal of Geophysical Research: Biogeosciences*, *118*, 1247–1255. https://doi.org/10.1002/jgrg.20100

Beer, C., Reichstein, M., Tomelleri, E., Ciais, P., Jung, M., Carvalhais, N., et al. (2010). Terrestrial gross carbon dioxide uptake: Global distribution and covariation with climate. *Science*, *329*(5993), 834–838. https://doi.org/10.1126/science.1184984

Bradford, M. A., & Crowther, T. W. (2013). Carbon use efficiency and storage in terrestrial ecosystems. *New Phytologist*, *199*(1), 7–9. https://doi.org/10.1111/nph.12334

Cai, W., Borlace, S., Lengaigne, M., Van Rensch, P., Collins, M., Vecchi, G., et al. (2014). Increasing frequency of extreme El Niño events due to greenhouse warming. *Nature Climate Change*, *4*(2), 111–116. https://doi.org/10.1038/nclimate2100

Cai, W., Santoso, A., Wang, G., Yeh, S.-W., An, S.-I., Cobb, K. M., et al. (2015). ENSO and greenhouse warming. *Nature Climate Change*, *5*(9), 849–859. https://doi.org/10.1038/nclimate2743

Campbell, J., Berry, J., Seibt, U., Smith, S. J., Montzka, S., Launois, T., et al. (2017). Large historical growth in global terrestrial gross primary production. *Nature*, *544*(7648), 84–87. https://doi.org/10.1038/nature22030

Chapin, F. S., Matson, P. A., & Mooney, H. A. (2002). Carbon input to terrestrial ecosystems. *Principles of Terrestrial Ecosystem Ecology*, 97–122. https://doi.org/10.1007/b97397

Chen, C., Cane, M. A., Henderson, N., Lee, D. E., Chapman, D., Kondrashov, D., & Chekroun, M. D. (2016). Diversity, nonlinearity, seasonality, and memory effect in ENSO simulation and prediction using empirical model reduction. *Journal of Climate*, *29*(5), 1809–1830. https://doi.org/10.1175/JCLI-D-15-0372.1

Chen, M., Parton, W. J., Del Grosso, S. J., Hartman, M. D., Day, K. A., Tucker, C. J., et al. (2017). The signature of sea surface temperature anomalies on the dynamics of semiarid grassland productivity. *Ecosphere*, *8*(12). https://doi.org/10.1002/ecs2.2069

Chen, Z., Yu, G., Zhu, X., Wang, Q., Niu, S., & Hu, Z. (2015). Covariation between gross primary production and ecosystem respiration across space and the underlying mechanisms: A global synthesis. *Agricultural and Forest Meteorology*, *203*, 180–190. https://doi.org/10.1016/j.agrformet.2015.01.012

Ciais, P., Piao, S.-L., Cadule, P., Friedlingstein, P., & Chédin, A. (2009). Variability and recent trends in the African terrestrial carbon balance. *Biogeosciences*, *6*(9), 1935–1948. https://doi.org/10.5194/bg-6-1935-2009

Collins, M., An, S.-I., Cai, W., Ganachaud, A., Guilyardi, E., Jin, F.-F., et al. (2010). The impact of global warming on the tropical Pacific Ocean and El Niño. *Nature Geoscience*, *3*(6), 391–397. https://doi.org/10.1038/ngeo868

Dai, A., & Wigley, T. (2000). Global patterns of ENSO-induced precipitation. *Geophysical Research Letters*, *27*(9), 1283–1286. https://doi.org/10.1029/1999GL011140

Dannenberg, M. P., Song, C., Hwang, T., & Wise, E. K. (2015). Empirical evidence of El Niño–Southern Oscillation influence on land surface phenology and productivity in the western United States. *Remote Sensing of Environment*, *159*, 167–180. https://doi.org/10.1016/j.rse.2014.11.026

Dannenberg, M. P., Wise, E. K., Janko, M., Hwang, T., & Smith, W. K. (2018). Atmospheric teleconnection influence on North American land surface phenology. *Environmental Research Letters*, *13*(3), 034029. https://doi.org/10.1088/1748-9326/aaa85a

Diaz, H. F., Hoerling, M. P., & Eischeid, J. K. (2001). ENSO variability, teleconnections and climate change. *International Journal of Climatology*, *21*(15), 1845–1862. https://doi.org/10.1002/joc.631

Friedl, M. A., McIver, D. K., Hodges, J. C., Zhang, X. Y., Muchoney, D., Strahler, A. H., et al. (2002). Global land cover mapping from MODIS: Algorithms and early results. *Remote Sensing of Environment*, *83*(1-2), 287–302. https://doi.org/10.1016/S0034-4257(02)00078-0

Friedlingstein, P. (2015). Carbon cycle feedbacks and future climate change. *Philosophical Transactions of the Royal Society A: Mathematical, Physical and Engineering Sciences*, *373*, 20140421. https://doi.org/10.1098/rsta.2014.0421

Gershunov, A., & Barnett, T. P. (1998). Interdecadal modulation of ENSO teleconnections. *Bulletin of the American Meteorological Society*, *79*(12), 2715–2725. https://doi.org/10.1175/1520-0477(1998)079<2715:IMOET>2.0.CO;2

Gonsamo, A., Chen, J. M., & Lombardozzi, D. (2016). Global vegetation productivity response to climatic oscillations during the satellite era. *Global Change Biology*, *22*(10), 3414–3426. https://doi.org/10.1111/gcb.13258

Guilyardi, E., Wittenberg, A., Fedorov, A., Collins, M., Wang, C., Capotondi, A., et al. (2009). Understanding El Niño in ocean–atmosphere general circulation models: Progress and challenges. *Bulletin of the American Meteorological Society*, *90*(3), 325–340. https://doi.org/10.1175/2008BAMS2387.1

Hashimoto, H., Nemani, R. R., White, M. A., Jolly, W. M., Piper, S. C., Keeling, C. D., et al. (2004). El Nino–Southern Oscillation–induced variability in terrestrial carbon cycling. *Journal of Geophysical Research-Atmospheres*, *109*(D23). https://doi.org/10.1029/2004JD004959

Hilker, T., Lyapustin, A. I., Tucker, C. J., Hall, F. G., Myneni, R. B., Wang, Y., et al. (2014). Vegetation dynamics and rainfall sensitivity of the Amazon. *Proceedings of the National Academy of Sciences*, *111*(45), 16,041–16,046. https://doi.org/10.1073/pnas.1404870111

Houghton, R. (2007). Balancing the global carbon budget. *Annual Review of Earth and Planetary Sciences*, *35*(1), 313–347. https://doi.org/10.1146/annurev.earth.35.031306.140057

Humphrey, V., Zscheischler, J., Ciais, P., Gudmundsson, L., Sitch, S., & Seneviratne, S. I. (2018). Sensitivity of atmospheric CO_2 growth rate to observed changes in terrestrial water storage. *Nature*, *560*(7720), 628–631. https://doi.org/10.1038/s41586-018-0424-4

Iizumi, T., Luo, J.-J., Challinor, A. J., Sakurai, G., Yokozawa, M., Sakuma, H., et al. (2014). Impacts of El Niño Southern Oscillation on the global yields of major crops. *Nature Communications*, *5*(1), 3712. https://doi.org/10.1038/ncomms4712

Jones, C. D., Collins, M., Cox, P. M., & Spall, S. A. (2001). The carbon cycle response to ENSO: A coupled climate–carbon cycle model study. *Journal of Climate*, *14*(21), 4113–4129. https://doi.org/10.1175/1520-0442(2001)014<4113:TCCRTE>2.0.CO;2

Jung, M., Reichstein, M., Schwalm, C. R., Huntingford, C., Sitch, S., Ahlström, A., et al. (2017). Compensatory water effects link yearly global land CO_2 sink changes to temperature. *Nature*, *541*(7638), 516–520. https://doi.org/10.1038/nature20780

Kim, J.-S., Kug, J.-S., & Jeong, S.-J. (2017). Intensification of terrestrial carbon cycle related to El Niño–Southern Oscillation under greenhouse warming. *Nature Communications*, *8*(1), 1674. https://doi.org/10.1038/s41467-017-01831-7

Kogan, F., & Guo, W. (2017). Strong 2015–2016 El Niño and implication to global ecosystems from space data. *International Journal of Remote Sensing*, *38*(1), 161–178. https://doi.org/10.1080/01431161.2016.1259679

Le Quéré, C., Andrew, R., Friedlingstein, P., Sitch, S., Pongratz, J., Manning, A., et al. (2018). Global Carbon Budget 2017. *Earth System Science Data*, *10*(1), 405–448. In. https://doi.org/10.5194/essd-10-405-2018

Liu, J., Bowman, K. W., Schimel, D. S., Parazoo, N. C., Jiang, Z., Lee, M., et al. (2017). Contrasting carbon cycle responses of the tropical continents to the 2015–2016 El Niño. *Science*, *358*(6360), eaam5690. https://doi.org/10.1126/science.aam5690

Luo, X., Keenan, T. F., Fisher, J. B., Jiménez-Muñoz, J.-C., Chen, J. M., Jiang, C., et al. (2018). The impact of the 2015/2016 El Nino on global photosynthesis using satellite remote sensing. *Philosophical Transactions of the Royal Society, B: Biological Sciences*, *373*(1760), 20170409. https://doi.org/10.1098/rstb.2017.0409

Luo, Y., Keenan, T. F., & Smith, M. (2015). Predictability of the terrestrial carbon cycle. *Global Change Biology*, *21*(5), 1737–1751. https://doi.org/10.1111/gcb.12766

MacBean, N., Maignan, F., Peylin, P., Bacour, C., Bréon, F.-M., & Ciais, P. (2015). Using satellite data to improve the leaf phenology of a global terrestrial biosphere model. *Biogeosciences*, *12*(23), 7185–7208. https://doi.org/10.5194/bg-12-7185-2015

McPhaden, M. J., Zebiak, S. E., & Glantz, M. H. (2006). ENSO as an integrating concept in earth science. *Science*, *314*(5806), 1740–1745. https://doi.org/10.1126/science.1132588

Migliavacca, M., Reichstein, M., Richardson, A. D., Colombo, R., Sutton, M. A., Lasslop, G., et al. (2011). Semiempirical modeling of abiotic and biotic factors controlling ecosystem respiration across eddy covariance sites. *Global Change Biology*, *17*(1), 390–409. https://doi.org/10.1111/j.1365-2486.2010.02243.x

Moore, C. E., Beringer, J., Donohue, R. J., Evans, B., Exbrayat, J. F., Hutley, L. B., & Tapper, N. J. (2018). Seasonal, interannual and decadal drivers of tree and grass productivity in an Australian tropical savanna. *Global Change Biology*, *24*(6), 2530–2544. https://doi.org/10.1111/gcb.14072

Parazoo, N. C., Barnes, E., Worden, J., Harper, A. B., Bowman, K. B., Frankenberg, C., et al. (2015). Influence of ENSO and the NAO on terrestrial carbon uptake in the Texas-northern Mexico region. *Global Biogeochemical Cycles*, *29*, 1247–1265. https://doi.org/10.1002/2015GB005125

Pettorelli, N., Vik, J. O., Mysterud, A., Gaillard, J.-M., Tucker, C. J., & Stenseth, N. C. (2005). Using the satellite-derived NDVI to assess ecological responses to environmental change. *Trends in Ecology & Evolution*, *20*(9), 503–510. https://doi.org/10.1016/j.tree.2005.05.011

Piao, S., Ciais, P., Friedlingstein, P., de Noblet-Ducoudré, N., Cadule, P., Viovy, N., & Wang, T. (2009). Spatiotemporal patterns of terrestrial carbon cycle during the 20th century. *Global Biogeochemical Cycles*, *23*, GB4026. https://doi.org/10.1029/2008GB003339

Power, S., Delage, F., Chung, C., Kociuba, G., & Keay, K. (2013). Robust twenty-first-century projections of El Niño and related precipitation variability. *Nature*, *502*(7472), 541–545. https://doi.org/10.1038/nature12580

Richardson, A. D., Anderson, R. S., Arain, M. A., Barr, A. G., Bohrer, G., Chen, G., et al. (2012). Terrestrial biosphere models need better representation of vegetation phenology: Results from the North American Carbon Program Site Synthesis. *Global Change Biology*, *18*(2), 566–584. https://doi.org/10.1111/j.1365-2486.2011.02562.x

Ropelewski, C. F., & Halpert, M. S. (1986). North American precipitation and temperature patterns associated with the El Niño/Southern Oscillation (ENSO). *Monthly Weather Review*, *114*(12), 2352–2362. https://doi.org/10.1175/1520-0493(1986)114<2352:NAPATP>2.0.CO;2

Running, S. W., Nemani, R. R., Heinsch, F. A., Zhao, M., Reeves, M., & Hashimoto, H. (2004). A continuous satellite-derived measure of global terrestrial primary production. *Bioscience*, *54*(6), 547–560. https://doi.org/10.1641/0006-3568(2004)054[0547:ACSMOG]2.0.CO;2

Seager, R., Kushnir, Y., Nakamura, J., Ting, M., & Naik, N. (2010). Northern Hemisphere winter snow anomalies: ENSO, NAO and the winter of 2009/10. *Geophysical Research Letters*, *37*, L14703. https://doi.org/10.1029/2010GL043830

Sitch, S., Friedlingstein, P., Gruber, N., Jones, S., Murray-Tortarolo, G., Ahlström, A., et al. (2015). Recent trends and drivers of regional sources and sinks of carbon dioxide. *Biogeosciences*, *12*(3), 653–679. https://doi.org/10.5194/bg-12-653-2015

Tippett, M. K., Barnston, A. G., & Li, S. (2012). Performance of recent multimodel ENSO forecasts. *Journal of Applied Meteorology and Climatology*, *51*(3), 637–654. https://doi.org/10.1175/JAMC-D-11-093.1

Vecchi, G. A., Clement, A., & Soden, B. J. (2008). Examining the tropical Pacific's response to global warming. *Eos, Transactions American Geophysical Union*, *89*(9), 81–83. https://doi.org/10.1029/2008EO090002

Viovy, N. (2018). CRUNCEP Version 7—Atmospheric Forcing Data for the Community Land Model. In *Research Data Archive at the National Center for Atmospheric Research*. Boulder, CO: Computational and Information Systems Laboratory. https://rda.ucar.edu/datasets/ds314.3/

Wang, C., & Picaut, J. (2004). Understanding ENSO physics—A review. *Earth's Climate: The Ocean–Atmosphere Interaction, Geophys. Monogr*, *147*, 21–48.

Wang, J., Zeng, N., Wang, M., Jiang, F., Wang, H., & Jiang, Z. (2018). Contrasting terrestrial carbon cycle responses to the 1997/98 and 2015/16 extreme El Niño events. *Earth System Dynamics*, *9*(1), 1–14. https://doi.org/10.5194/esd-9-1-2018

Wang, X., Piao, S., Ciais, P., Friedlingstein, P., Myneni, R. B., Cox, P., et al. (2014). A two-fold increase of carbon cycle sensitivity to tropical temperature variations. *Nature*, *506*(7487), 212–215. https://doi.org/10.1038/nature12915

Waring, R. H., & Running, S. W. (2010). *Forest ecosystems: Analysis at multiple scales*. San Diego, CA: Elsevier Academic Press.

Welp, L. R., Keeling, R. F., Meijer, H. A., Bollenbacher, A. F., Piper, S. C., Yoshimura, K., et al. (2011). Interannual variability in the oxygen isotopes of atmospheric CO_2 driven by El Niño. *Nature*, *477*(7366), 579–582. https://doi.org/10.1038/nature10421

Wise, E. K. (2010). Spatiotemporal variability of the precipitation dipole transition zone in the western United States. *Geophysical Research Letters*, *37*, L07706. https://doi.org/10.1029/2009GL042193

Wise, E. K., Wrzesien, M. L., Dannenberg, M. P., & McGinnis, D. L. (2015). Cool-season precipitation patterns associated with teleconnection interactions in the United States. *Journal of Applied Meteorology and Climatology*, *54*(2), 494–505. https://doi.org/10.1175/JAMC-D-14-0040.1

Woodward, F., Lomas, M., & Quaife, T. (2008). Global responses of terrestrial productivity to contemporary climatic oscillations. *Philosophical Transactions of the Royal Society of London B: Biological Sciences*, *363*(1504), 2779–2785. https://doi.org/10.1098/rstb.2008.0017

Wu, R., Hu, Z.-Z., & Kirtman, B. P. (2003). Evolution of ENSO-related rainfall anomalies in East Asia. *Journal of Climate*, *16*(22), 3742–3758. https://doi.org/10.1175/1520-0442(2003)016<3742:EOERAI>2.0.CO;2

Yeh, S. W., Cai, W., Min, S. K., McPhaden, M. J., Dommenget, D., Dewitte, B., et al. (2018). ENSO atmospheric teleconnections and their response to greenhouse gas forcing. *Reviews of Geophysics*, *56*(1), 185–206. https://doi.org/10.1002/2017RG000568

Zhang, A., Jia, G., Epstein, H. E., & Xia, J. (2017). ENSO elicits opposing responses of semi-arid vegetation between Hemispheres. *Scientific Reports*, *7*, 42281. https://doi.org/10.1038/srep42281

Zhang, X., Wang, Y. P., Peng, S., Rayner, P. J., Ciais, P., Silver, J. D., et al. (2018). Dominant regions and drivers of the variability of the global land carbon sink across timescales. *Global Change Biology*, *24*(9), 3954–3968. https://doi.org/10.1111/gcb.14275

Zhang, Y., Song, C., Band, L.E. & Sun, G. (2019). No proportional increase of terrestrial gross carbon sequestration from the greening Earth. *Journal of Geophysical Research: Biogeosciences, 124*, 1–13. https://doi.org/10.1029/2018JG004917

Zhang, Y., Song, C., Sun, G., Band, L. E., Noormets, A., & Zhang, Q. (2015). Understanding moisture stress on light use efficiency across terrestrial ecosystems based on global flux and remote-sensing data. *Journal of Geophysical Research: Biogeosciences*, *120*, 2053–2066. https://doi.org/10.1002/2015JG003023

Zhang, Y., Song, C., Sun, G., Band, L. E., McNulty, S., Noormets, A., et al. (2016). Development of a coupled carbon and water model for estimating global gross primary productivity and evapotranspiration based on eddy flux and remote sensing data. *Agricultural and Forest Meteorology*, *223*, 116–131. https://doi.org/10.1016/j.agrformet.2016.04.003

Zhao, L., Dai, A., & Dong, B. (2018). Changes in global vegetation activity and its driving factors during 1982–2013. *Agricultural and Forest Meteorology*, *249*, 198–209. https://doi.org/10.1016/j.agrformet.2017.11.013

Zhu, Z., Bi, J., Pan, Y., Ganguly, S., Anav, A., Xu, L., et al. (2013). Global data sets of vegetation leaf area index (LAI) 3g and Fraction of Photosynthetically Active Radiation (FPAR) 3g derived from Global Inventory Modeling and Mapping Studies (GIMMS) Normalized Difference Vegetation Index (NDVI3g) for the period 1981 to 2011. *Remote Sensing*, *5*, 927–948.

Zhu, Z., Piao, S., Xu, Y., Bastos, A., Ciais, P., & Peng, S. (2017). The effects of teleconnections on carbon fluxes of global terrestrial ecosystems. *Geophysical Research Letters*, *44*, 3209–3218. https://doi.org/10.1002/2016GL071743